The Astrophysical Journal, 928:143 (17pp), 2022 April 1 https://doi.org/10.3847/1538-4357/ac559c

A Search for Correlations between Turbulence and Star Formation in THINGS Galaxies

Bruce G. Elmegreen[1], Zorayda Martinez[2,3], and Deidre A. Hunter[2]
[1] IBM T. J. Watson Research Center, 1101 Kitchawan Road, Yorktown Heights, NY 10598, USA
[2] Lowell Observatory, 1400 West Mars Hill Road, Flagstaff, AZ 86001, USA
[3] Department of Astronomy and Planetary Science, Northern Arizona University, 527 S. Beaver Street, Flagstaff, AZ 86011, USA
Received 2021 October 7; revised 2022 January 29; accepted 2022 February 14; published 2022 April 4

Abstract

The spatial range for feedback from star formation varies from molecular cloud disruption on parsec scales to supershells and disk blowout on kiloparsec scales. The relative amounts of energy and momentum given to these scales are important for understanding the termination of star formation in any one region and the origin of interstellar turbulence and disk stability in galaxies as a whole. Here, we measure, for 11 THINGS galaxies, the excess kinetic energy, velocity dispersion, and surface density of H I gas associated with regions of excess star formation, where the excess is determined from the difference between the observed local value and the azimuthal average. We find small decreases in the excess kinetic energy and velocity dispersion in regions of excess star formation rate density, suggesting that most of the feedback energy does not go into local H I motion. Most likely, it disrupts molecular clouds and dissipates rapidly at high gas density. Some could also be distributed over larger regions, filling in spaces between the peaks of star formation and contributing to other energy sources from self-gravity and spiral arm shocks.

Unified Astronomy Thesaurus concepts: Interstellar atomic gas (833); Star forming regions (1565); Stellar feedback (1602)

1. Introduction

Energy from massive stars in the form of ionization, radiation pressure, winds, and supernovae drives gas expansion and turbulence in the neighborhoods of star formation, disrupting the associated molecular clouds (e.g., Chevance et al. 2020) and powering lower-density gas around them (e.g., Nath et al. 2020). An important quantity is the fraction of turbulence this feedback powers. Other potential sources of turbulence have been known for a long time. They include disk instabilities driven by gravity (de Vega et al. 1996; Bertin & Lodato 2001; Gammie 2001; Huber & Pfenniger 2001; Vollmer & Beckert 2002; Wada et al. 2002; Elmegreen et al. 2003; Krumholz & Burkert 2010), vertical and in-plane instabilities driven by magnetism (Parker 1966; Asseo et al. 1978; Balbus & Hawley 1991; Sellwood & Balbus 1999; Kim et al. 2003; Piontek & Ostriker 2007), thermal instabilities (Hennebelle & Audit 2007; Gazol & Kim 2010), galactic shear (Richard & Zahn 1999; Semelin & Combes 2000), and energy coming from outside the disk, such as via gas accretion (Tenorio-Tagle 1981; Elmegreen & Burkert 2010) and galaxy interactions (Elmegreen et al. 1993; Kaufman et al. 1997; Goldman 2000; Burkhart et al. 2010; Ashley et al. 2013; Renaud et al. 2014). General reviews on the origins of interstellar turbulence can be found in Elmegreen & Scalo (2004) and Mac Low & Klessen (2004).

If a large fraction of interstellar turbulence is driven by young stellar feedback, then star formation may regulate itself by inflating the disk and lowering the density when the star formation rate is high (Goldreich & Lynden-Bell 1965; Franco & Shore 1984; Ostriker et al. 2010). If feedback is unable to power a high fraction of the disk, then large-scale turbulence and marginal disk stability may need another driver, such as self-gravity (Li et al. 2005), which grows more active in inverse relation with the turbulent speed via the Toomre Q parameter (Kim et al. 2002; Kim & Ostriker 2007).

A combination of these processes with different fractions in different places is likely. Some observations suggest that gravity or magnetic instabilities dominate turbulence generation at a low star formation rate density (SFRD), $\leqslant 10^{-9} M_\odot$ pc^{-2} yr^{-1}, while feedback dominates at high SFRD (Agertz et al. 2009; Tamburro et al. 2009). Models by Kim et al. (2013) suggest that feedback controls turbulence and the SFRD in the outer disk where the SFRD is low. The observations for local galaxies can be ambiguous. An observed correlation between gas velocity dispersion and SFRD could be the result of correlations between each quantity and galactocentric radius (e.g., Stilp et al. 2013a) with no mutual correlation between them. Also, the lack of a correlation between turbulence and SFRD could be the result of sampling the SFRD at the wrong time (Stilp et al. 2013). Feedback could also dominate turbulence on small scales while self-gravity dominates it on large scales (Joung et al. 2009).

HI turbulence properties have also been examined using power spectra of the emission. Zhang et al. (2012) found no correlation between the power spectral index and the average galaxy SFRD for 24 dwarf irregular galaxies. Szotkowski et al. (2019) found no correlation between the local spectral index and SFRD in the Small Magellanic Cloud. Both papers suggested that turbulence driving comes from larger scales than star-forming regions. For the Large Magellanic Cloud, Szotkowski et al. (2019) measured a steeper-than-average slope around the giant star-forming region 30 Doradus, suggesting that feedback could have destroyed the small-scale structure.

Numerical simulations of turbulence in an interstellar patch show that supernovae and other types of feedback can give the observed velocity dispersion and scale height (Norman & Ferrara 1996; Avila-Reese & Vázquez-Semadeni 2001; de Avillez & Breitschwerdt 2005; Dib et al. 2006). This does

Table 1
The Galaxy Sample

Galaxy	Type	D[a] (Mpc)	H I RO Beam[b] Major (″)	H I RO Beam[b] Minor (″)	Inclination[c] (°)	PA[d] (°)	Center[e] R.A. (^{h}: ^{m}. ^{s})	Center[e] Decl. (°:′:″)
DDO 154	dIrr	3.7	7.94	6.27	65.2	46.0	12:54:06.25	+27:09:02.0
NGC 925	Sd	9.2	4.85	4.65	66.0	286.6	02:27:16.5	+33:34:43.5
NGC 2403	Scd	3.2	6.01	5.17	62.9	123.7	07:36:51.1	+65:36:02.9
NGC 2841	Sb	14.1	6.06	5.79	73.7	152.6	09:22:02.6	+50:58:35.4
NGC 2976	Sc	3.6	5.25	4.88	64.5	334.5	09:47:15.3	+67:55:00.0
NGC 3198	Sc	13.8	7.64	5.62	71.5	215.0	10:19:55.0	+45:32:58.9
NGC 4736	Sab	4.7	5.96	5.55	41.4	296.1	12:50:53.0	+41:07:13.2
NGC 5055	Sbc	10.1	5.78	5.26	59.0	101.8	13:15:49.2	+42:01:45.3
NGC 6946	Scd	5.9	4.93	4.51	32.6	242.7	20:34:52.2	+60:09:14.4
NGC 7331	Sb	14.7	4.94	4.60	75.8	167.7	22:37:04.1	+34:24:56.5
NGC 7793	Sd	3.9	10.37	5.39	49.6	290.1	23:57:49.7	−32:35:27.9

Notes.
[a] Distance to the galaxy from Walter et al. (2008).
[b] The major and minor beam sizes as presented in Walter et al. (2008).
[c] The inclination of the galaxies in degrees (de Blok et al. 2008).
[d] Position angle of the galaxy in degrees from de Blok et al. (2008).
[e] Center of the galaxy in RA and Dec as given in Trachternach et al. (2008).

Table 2
Constants

Galaxy	Mass Conversion Factor[a] (10^{19} atom cm^{-2} (Jy beam^{-1} m s^{-1})$^{-1}$)	Σ_{HI} Calibration[b] ($M_\odot$ pc^{-2} (Jy beam^{-1} m s^{-1})$^{-1}$)	KED Calibration[c] (10^{43} ergs pc^{-2})	ΔR[d] (″)
DDO 154	2.220	0.1780	2.371×10^{-7}	6
NGC 925	4.900	0.3926	5.232×10^{-7}	50
NGC 2403	3.556	0.2850	3.798×10^{-7}	60
NGC 2841	3.149	0.2524	3.363×10^{-7}	60
NGC 2976	4.313	0.3456	4.606×10^{-7}	50
NGC 3198	2.574	0.2062	2.748×10^{-7}	60
NGC 4736	3.341	0.2677	3.567×10^{-7}	50
NGC 5055	3.635	0.2912	3.881×10^{-7}	50
NGC 6946	4.970	0.3982	5.307×10^{-7}	50
NGC 7331	4.863	0.2294	3.057×10^{-7}	50
NGC 7793	1.977	0.1584	2.111×10^{-7}	70

Notes.
[a] Conversion constant for converting the moment 0 map into units of atom cm^{-2}.
[b] Conversion factor that puts the moment 0 map into units of $M_\odot$ pc^{-2}.
[c] A factor to convert the moment 0 × (moment 2)^2 maps into units of ergs pc^{-2}.
[d] Width of the annuli used in determining the radial profiles as described in Section 2.3.

not necessarily mean that the large-scale velocity dispersion varies with SFRD. Joung & Mac Low (2006) found that most of the feedback energy is deposited within a few hundred pc of the energy source. Joung et al. (2009) also show that, even with only feedback to excite the gas, the mass-weighted velocity dispersion (which is similar to the kinetic energy density discussed below) and the simulated H I linewidths do not change much with SFRD when higher SFRDs correspond to higher gas surface densities according to the Kennicutt–Schmidt relation. Moreover, turbulence in an interstellar patch cannot capture larger-scale processes like gravitational instabilities (Balbus & Papaloizou 1999) or spiral shocks unless they are included specifically, and then these processes may dominate turbulence driving, as found by Kim et al. (2006, 2010). For example, spiral shocks in M51 have enormous peculiar speeds, 50 km s^{-1} in some regions (Shetty et al. 2007), suggesting that these shocks are a good source of turbulent motions.

If disk gravity maintains $Q \sim 1$ through spiral instabilities and gas collapse into clouds, then the turbulent speed is partly defined by that condition, i.e., it depends on the effective mass surface density and epicyclic frequency (e.g., Goldbaum et al. 2016). Simulations by Bournaud et al. (2010) modeled this case to fit the infrared dust power spectrum of the Large Magellanic Cloud and pointed out that feedback was necessary primarily to prevent the accumulation of gas in very dense clumps, which was a runaway process with only gravity present. Hopkins et al. (2011) also found that the disruption of dense gas was the most important role of feedback, and that without it, the SFR would be higher by a factor of 100. Hennebelle & Iffrig (2014) also found that supernovae clustered in regions of star formation lower the star formation rate by a factor of 30 compared to random supernovae, emphasizing again the importance of dense gas disruption in feedback control. Combes et al. (2012) simulated the power spectrum in M33 and also noted that feedback primarily

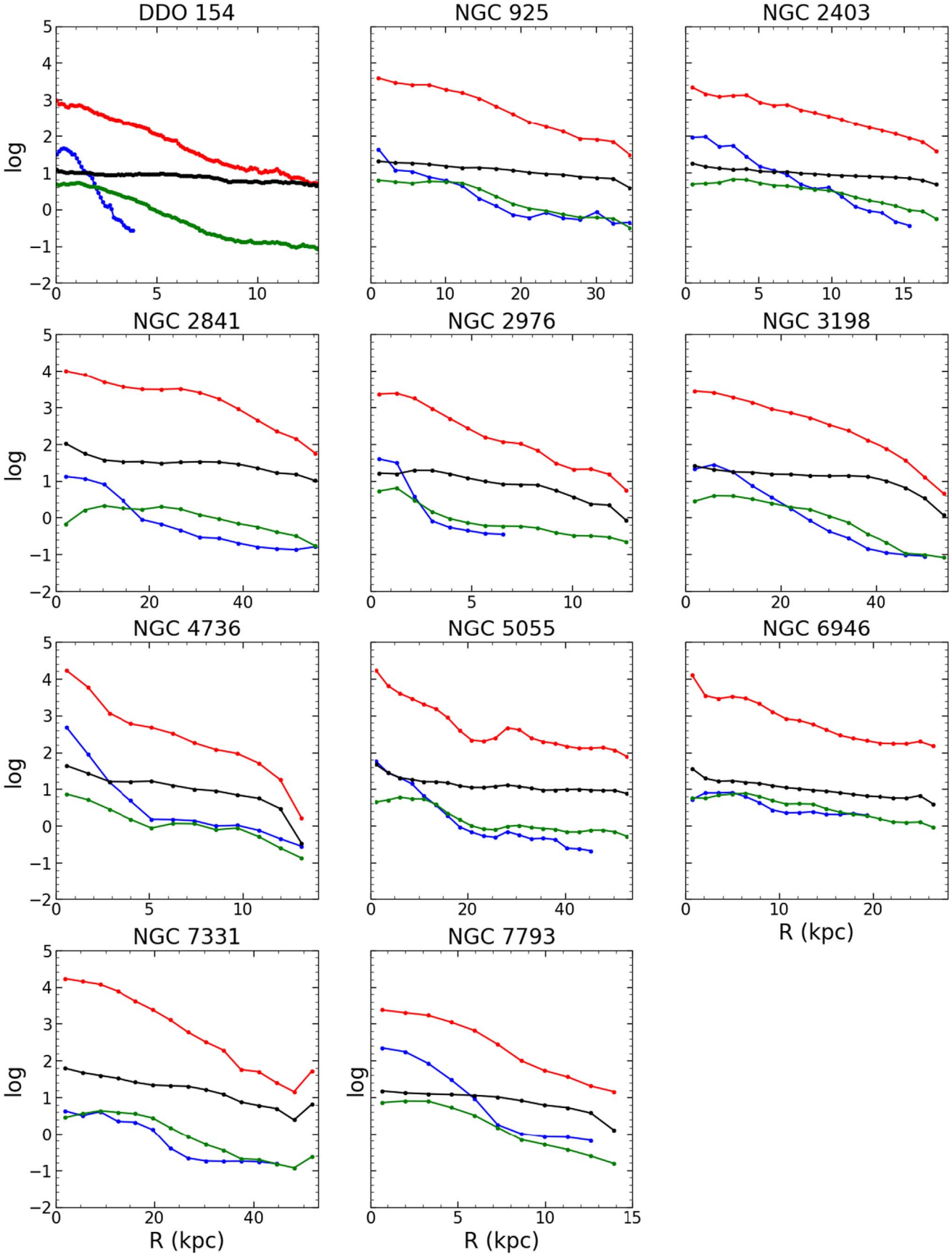

Figure 1. Azimuthally averaged radial profiles created as described in Section 2.3. Red curves are log KED in units of 10^{43} ergs pc^{-2}, black curves are log $V_{\rm disp}$ in units of km s^{-1}, green curves are log $\Sigma_{\rm HI}$ in units of $M_\odot$ pc^{-2}, and blue curves are log SFR/area in units of 10^{-10} $M_\odot$ pc^{-2} yr^{-1}. The plotted SFRD is limited by the extent of the FUV.

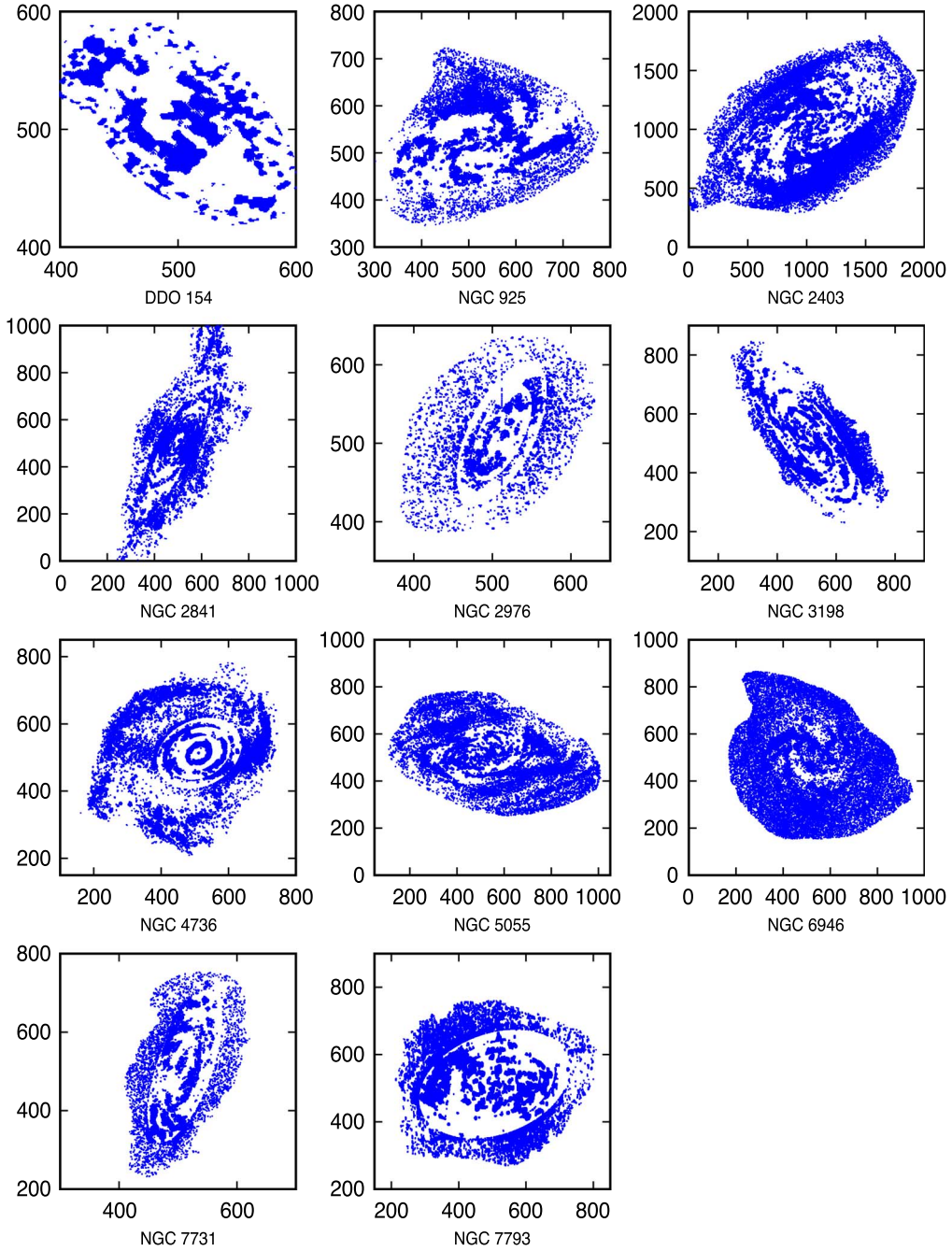

Figure 2. Distributions of pixels with positive values of SFRD, used for the determination of excess KED, $V_{\rm disp}$, and $\Sigma_{\rm HI}$ as functions of excess SFRD. Units on the axes are pixels, which are $1\farcs5$ across for all galaxies but NGC 2403, where they are $1\farcs0$.

influenced the high-frequency regime and was necessary to correctly get that part of the power spectrum and the associated inflection point (from two-dimensional turbulence to three-dimensional turbulence). Walker et al. (2014) reproduced the power spectra of galaxies in the THINGS survey with high-feedback models, as weak feedback gave too shallow a power spectrum, i.e., too much small-scale power.

More recent simulations of THINGS galaxy power spectra by Grisdale et al. (2017) show that feedback can influence a wide range of scales, up to 1–2 kpc, which is more than the disk thickness. As in the previous work, too little feedback increased the high-frequency structure and flattened the power spectrum there. They also point out that large-scale gravity is important as well, because without it, the power spectrum is too shallow on large scales, i.e., there is too little large-scale structure.

Resolved galaxies in cosmological simulations by Orr et al. (2020) showed little correlation between gas velocity dispersion and SFRD although they noted the importance of feedback on turbulence for timescales longer than the age of a star-forming region. In agreement with this, Hunter et al. (2022) found a correlation between elevated interstellar turbulence and star formation that occurred 100 to 200 Myr ago, but not star formation at shorter or longer timescales.

Evidently, both disk gravity and its activity prior to or independent of star formation, plus feedback after star formation, are essential to reproduce observed gas structures and motions

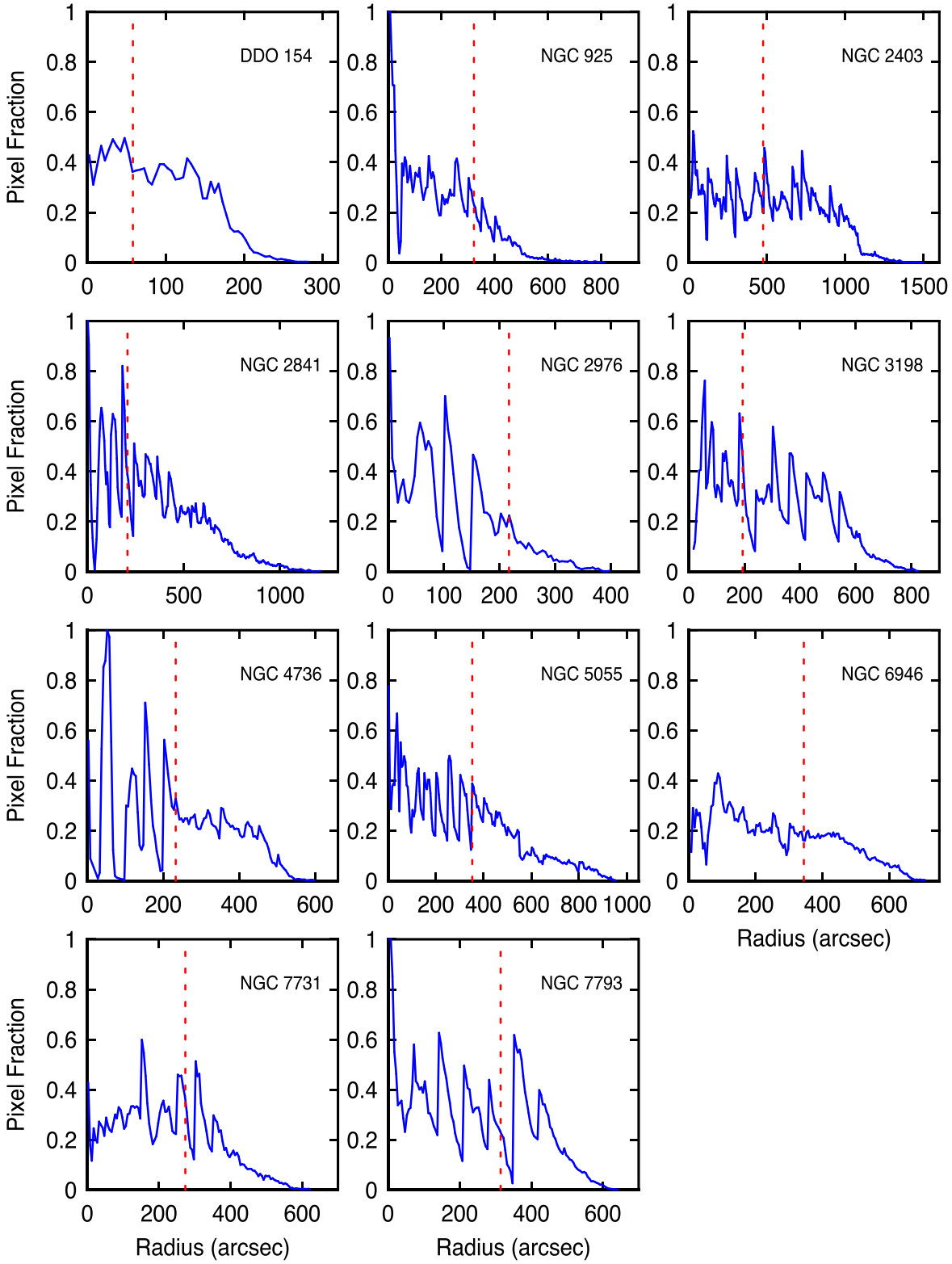

Figure 3. The fraction of pixels as a function of radius that are used for the calculation of the excess values. The vertical red dotted line is the isophotal radius R_{25}.

throughout galaxy disks. Both may be required for the regulation of star formation also, even though either one alone can give the right star formation rate and turbulence speed with reasonable parameters. This blend of distinct processes makes it difficult to find the boundary between them, whether measured as the scale separating large-scale gravity and small-scale star formation effects, or as the relative contribution of each to turbulence generation and self-regulation.

In this paper, we examine the excess H I turbulence in localized regions of star formation by removing the average radial profiles of each. Turbulence is measured by the kinetic energy density, KED, and by the second moment of the H I

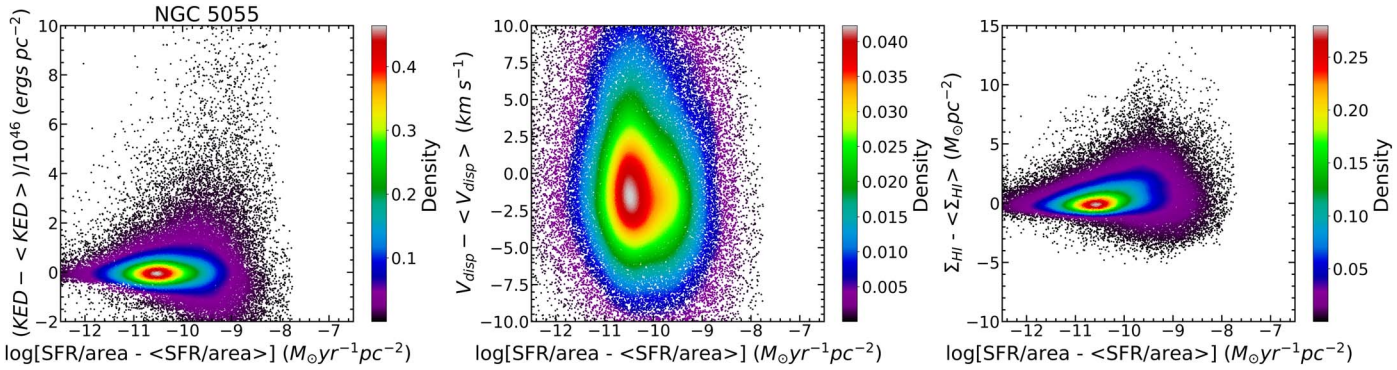

Figure 4. Pixel–pixel plots showing the excess KED in units of 10^{46} erg pc^{-2}, $V_{\rm disp}$ in km s^{-1}, and $\Sigma_{\rm HI}$ in $M_\odot$ pc^{-2} against the log of the excess SFRD in $M_\odot$ pc^{-2} yr^{-1}. The excess is defined to be the difference between the local values and the values from the average radial profiles. The color scale represents the density of points. NGC 5055 is shown here for illustration; the other galaxies are shown in the Appendix.

spectra. We also measure excess H I column density as a function of excess SFRD. The goal is to estimate the fraction of star formation feedback energy that goes into H I turbulence locally. If this fraction is low, then this energy either spreads out quickly from each star formation site, so there is little excess energy density there, or the energy is dissipated almost entirely in phases and scales of the interstellar medium that are not observed with H I, such as molecular clouds.

2. Data

2.1. Galaxy Sample

The 11 galaxies used here, 10 spirals and one dIrr, were drawn from THINGS (Walter et al. 2008), a large H I survey of nearby galaxies using the Very Large Array (VLA[4]). The THINGS H I emission maps are available for download, and we used the robust-weighted integrated H I (moment 0) and velocity dispersion (moment 2) maps. The pixel scale is 1.″5 except for NGC 2403, which has a pixel scale of 1.″0.

To quantify the star formation rate density, we used far-ultraviolet (FUV) images taken with the NASA Galaxy Evolution Explorer (GALEX; Martin et al. 2005). These images, obtained from the GALEX archives, were geometrically transformed and smoothed to the H I map orientation, pixel scale, and resolution so that the images could be directly compared. The native resolution of GALEX FUV imagery is $\sim 4''$.

The sample galaxies and basic properties are given in Table 1.

2.2. Creating Images

For the GALEX FUV images, foreground and background objects were removed and replaced with an average of the noise in a two-pixel-wide annulus around the object using the IMEDIT tool in the Image Reduction and Analysis Facility (IRAF; Tody 1986). We used IMSURFIT to construct a two-dimensional fit to the sky and subtract it from the cleaned FUV image. Pixels outside of the galaxy determined by eye were blanked using the task BLANK in the Astronomical Image Processing System developed by NRAO in order to prevent noise from affecting the pixel–pixel comparisons.

[4] The VLA is a facility of the National Radio Astronomy Observatory. The National Radio Astronomy Observatory is a facility of the National Science Foundation operated under cooperative agreement by Associated Universities, Inc.

The moment 0 (MOM0) map became the H I mass surface density ($\Sigma_{\rm HI}$), the moment 2 (MOM2) map became the velocity dispersion ($V_{\rm disp}$), and the FUV image became the star formation rate per area, called here the star formation rate density (SFRD). The kinetic energy density (KED) was constructed from $0.5 \times \Sigma_{\rm HI} \times V_{\rm disp}^2$. The units for the four quantities are 10^{43} ergs pc^{-2} for KED, km s^{-1} for $V_{\rm disp}$, $M_\odot$ pc^{-2} for $\Sigma_{\rm HI}$, and 10^{-10} $M_\odot$ pc^{-2} yr^{-1} for SFRD. The KED was corrected for the presence of He and heavy elements in the galaxy using $1.34 \times \Sigma_{\rm HI}$. The conversion factor used for transforming the MOM0 map units of Jy beam^{-1} m s^{-1} to atoms cm^{-2} is given in Table 2. To convert FUV flux to an SFRD, we used SFRD $= {\rm FUV}/10^{6.466}$, derived from Kennicutt (1998) for the spirals and for the dwarf DDO 154 SFRD $= {\rm FUV}/10^{6.508}$, as given by Hunter et al. (2010).

The moment 2 value of the H I line profile, rather than the FWHM, is used to probe HI turbulence because MOM2 contains more information about the line wings, making it a more sensitive measure of excess motion. MOM2 is also a better measure of kinetic energy (Tamburro et al. 2009). We are looking for any indication that star formation energizes the local atomic gas, and this could include high-speed motions in shells or other disturbances that appear in the line wings.

High-speed shear, compression, and expansion from spiral density waves could also contribute to MOM2 values inside the $\sim 6''$ H I beam. This angular size corresponds to several hundred parsecs for the more distant galaxies. These contributions to MOM2 will increase the measured velocity dispersions mostly in the arms where there are spiral density wave shocks, but they should not contribute much between the arms or in quiescent regions where the gas flows more smoothly. As a result, the average value of MOM2 used for background subtraction could be a little less than the background value in the arms, and thus the difference between the MOM2 values in star-forming regions, which are mostly in the arms, and the average background could be somewhat higher than it would be without spiral arm streaming motions. For this reason, the excess $V_{\rm disp}^2$ and KED values associated with regions of excess star formation should be considered upper limits to the effects of feedback. Because the excess $V_{\rm disp}^2$ and KED are already low (see below), the feedback energy going into H I should be even lower than what our results suggest.

The physical contributions to $V_{\rm disp}^2$ measured from MOM2 could also vary from region to region or between galaxies. Some regions with locally high excess $V_{\rm disp}^2$ could contain expanding H I shells with significant feedback energy into the local H I. Other regions with low or negative excess $V_{\rm disp}^2$ could

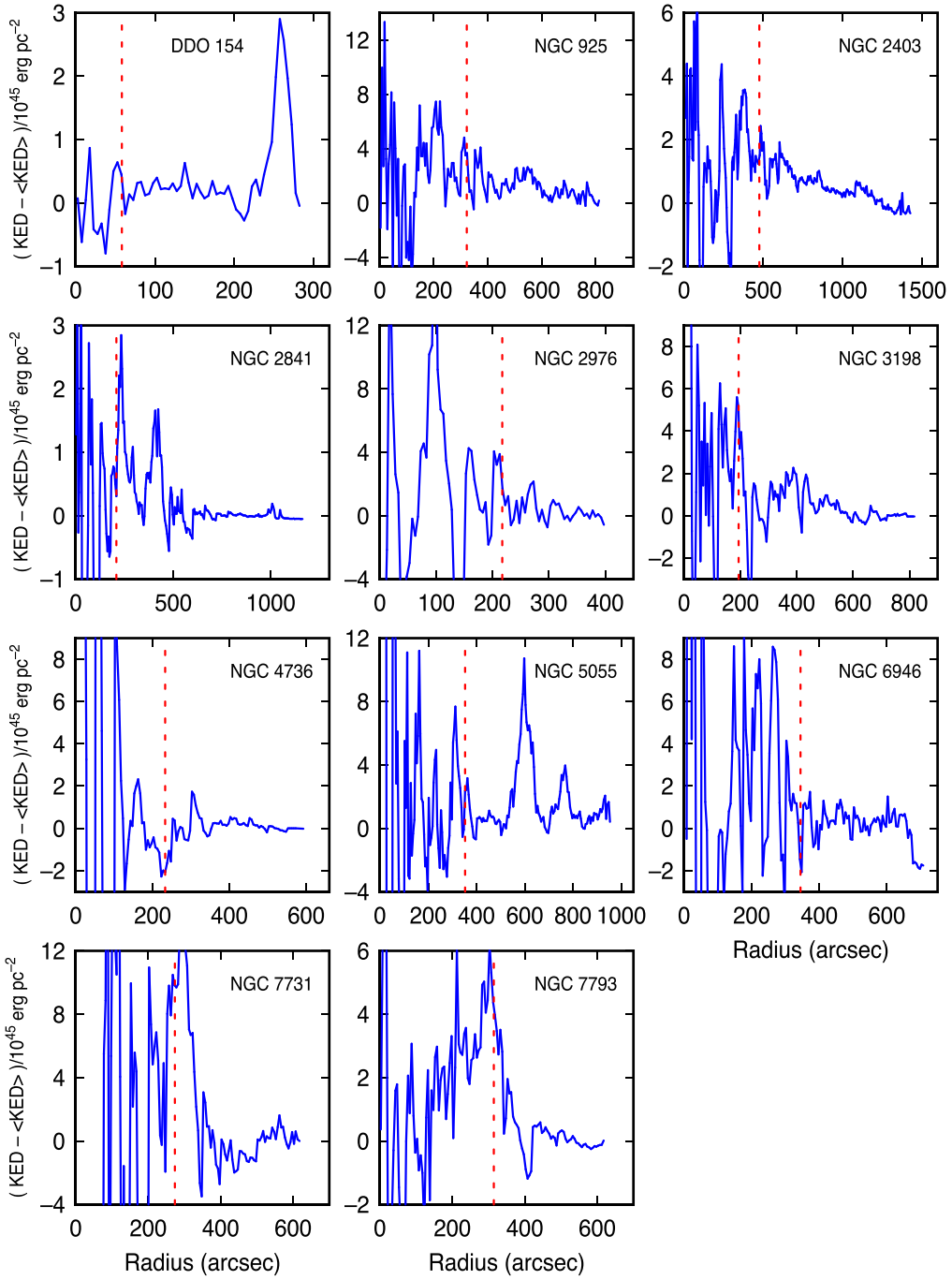

Figure 5. The excess KED in H I, in units of 10^{45} erg pc^{-2}, is shown as a function of galactocentric radius in arcsec. The vertical dotted line is the optical radius, R_{25}.

have a different star formation age or another destination for the stellar energy and momentum. Here, we consider the average trends of excess KED and $V_{\rm disp}^2$ versus excess SFRD as a measure of the global effects of feedback on the local atomic medium.

2.3. Radial Profiles

We are interested in the relation between H I turbulence and local star formation. Because there could be several sources of H I turbulence, we consider only the local excess MOM2 above its average radial value and examine this excess as a function of the excess SFRD above the SFRD average radial value. If local star formation drives local turbulence, then there should be a positive correlation between these excess values. The H I quantities come from maps that have full coverage in each disk, even between and beyond the star-forming regions, but the SFRD is too low to measure in some places, as star formation is generally patchy. We consider the H I excesses only in regions where the SFRD can be measured. Thus, the average radial values for H I come from everywhere and are representative of all the H I as a function of radius, but the local excesses above these averages come from the star-forming regions.

Determining the radial profiles of the sample involves superposing elliptical annuli onto the images in order to cover the majority of the signal in both the SFRD image and the

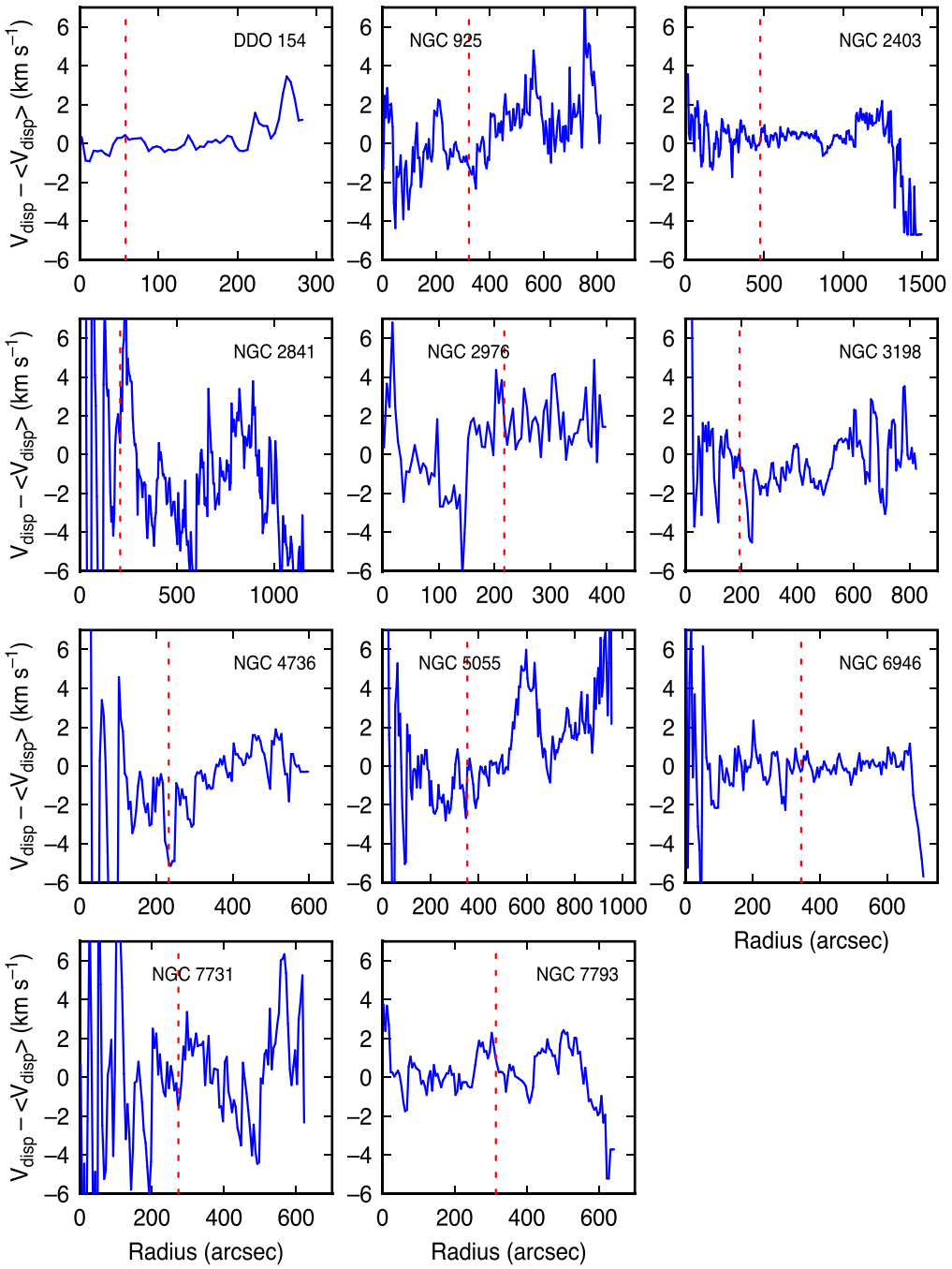

Figure 6. The excess MOM2 velocity dispersion for H I, in units of km s^{-1}, is shown as a function of galactocentric radius in arcsec. The vertical dotted line is the optical radius, R_{25}.

images derived from the H I maps. (Note that the H I maps extend significantly farther than the FUV emission in all galaxies). The center of each galaxy and the position angle of the major axis are given in Table 1. The inclination of the galaxy was used to derive the minor-to-major axis ratio b/a of the ellipses, assuming that the intrinsic b/a due to the thickness of the disk of spirals is 0.2 while that of dwarfs is 0.3 (Hodge & Hitchcock 1966). Approximately 10 times the H I beam size was used as the width of the annuli, ΔR, which is given in Table 2. This gives annuli wide enough to contain a statistically significant area, but not so large that the annulus extends over a region where the exponential disk drops off significantly. This judgement was made by eye. The exception to this was DDO 154, where we used an annulus width of 6″ to match the radial profiles in Hunter et al. (2012). Quantities were also corrected to face-on by multiplying the flux per pixel by the cosine of the inclination of the galaxy. The resulting average radial profiles are shown in Figure 1. There are no obvious features corresponding to spiral arms in the optical disk. To determine the excesses by subtracting the appropriate average from each pixel value, we found the distance of each pixel from the center of the galaxy in the plane of the disk and assigned this distance to the correct annulus.

Each annulus used to create the radial profile was checked for the number of SFRD pixels. Toward the outer galaxy, there may be many values of KED, Σ_{HI}, or V_{disp}, but a statistically less

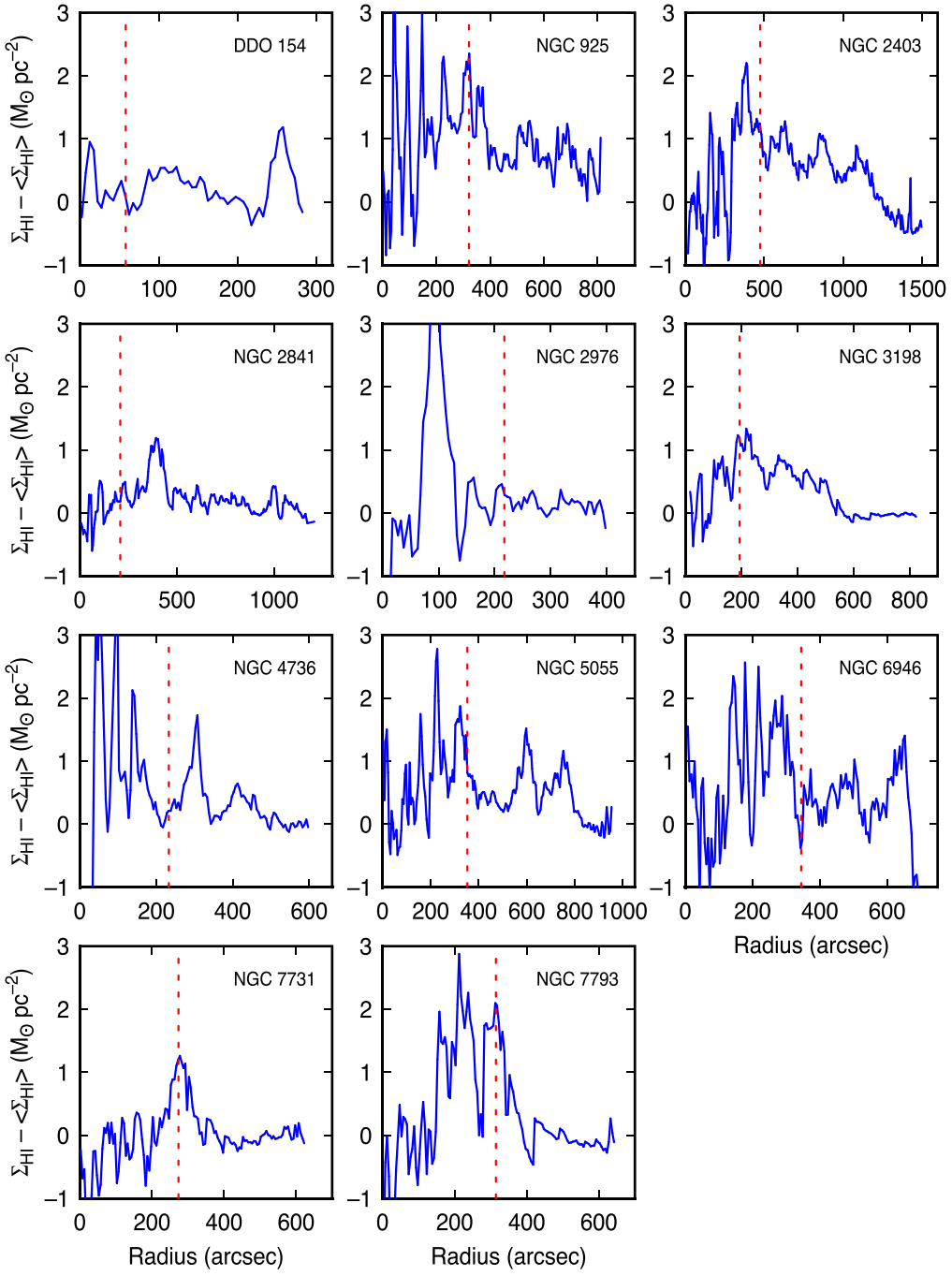

Figure 7. The excess surface density of H I, in units of $M_\odot$ pc^{-2}, is shown as a function of galactocentric radius in arcsec. The vertical dotted line is the optical radius, R_{25}.

significant number of values for SFRD. In order to maintain a lower uncertainty in the averages, annuli that contained less than 100 pixels in the SFRD were not plotted. Maps showing all of the pixels with measured SFRD are shown in Figure 2; there are traces of spiral structure because the SFRD is highest there. The fraction of pixels that are included for the excess SRFD values is in Figure 3. This fraction ranges between 0.2 and 0.4 inside R_{25} and tapers off beyond 1.5–2 R_{25}.

2.4. Pixel–Pixel Plots

Each pair of values of an excess quantity in a pixel, such as the excess KED and the corresponding excess SFRD, was plotted as a point in the two-dimensional plane of these quantities. The density of these points on the plane shows the probability distribution function for the correlation between values. We refer to these plots as pixel–pixel plots. In constructing these plots, we first eliminated pixels from the total KED, Σ_{HI}, V_{disp}, and SFRD maps with values less than or equal to zero, as they represent blanked pixels. Then, for each of the nonzero pixels, the annular average value at that position determined from all the pixels in the annulus, including the negative pixels, was subtracted from the positive pixel value to give the excess value. We fit the resulting pixel–pixel plots with a color density scale that shows the locations of highest pixel densities. NGC 5055 is shown for illustration in Figure 4. The rest of the galaxies are shown in Figures 12–14 in the Appendix.

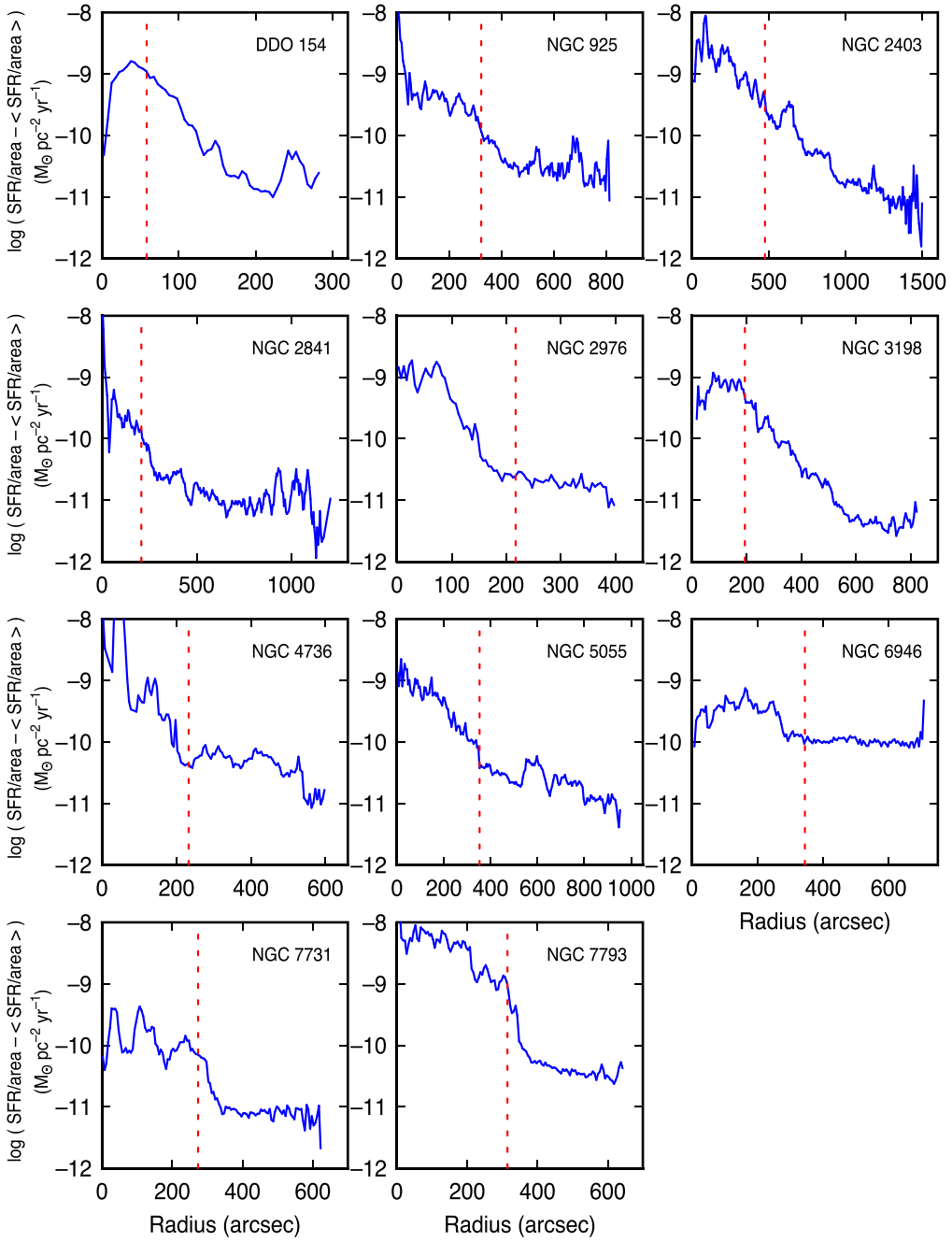

Figure 8. The excess star formation rate density, SFR/Area, in units of $M_{\odot}$ pc^{-2} yr^{-1}, is shown as a function of galactocentric radius in arcsec. The vertical dotted line is the optical radius, R_{25}.

Radial profiles of the average excess values are in Figures 5–8. The optical radius R_{25} is indicated by a vertical dotted red line. The velocity dispersion excess generally increases with radius, and the $\Sigma_{\rm HI}$ excess decreases a little with radius. These changes in these two quantities offset each other, to make the KED excess about constant. The excess SFRD decreases strongly with radius, like the average exponential disk itself, suggesting that star-forming regions are selected to be at a fixed multiplicative threshold above the average FUV disk. For this reason, pixels with large excess SFRD in the pixel–pixel plots tend to be in the inner disks. The large excesses in KED and $\Sigma_{\rm HI}$ at 260″ in DDO 154 and 600″ in NGC 5055 are well beyond the optical radii.

There is sometimes a correspondence between the excursions in these figures. There is a large bump at 100″ in NGC 2976 for both excess $\Sigma_{\rm HI}$ and KED, which probably corresponds to large H I clouds in the southwest and northeast, as shown in Figure 25 of Walter et al. (2008). This bump is not present for excess $V_{\rm disp}$ nor SFRD. This difference implies that the excess KED is from the surface density part of this quantity, not the velocity dispersion part. NGC 6946 also has a bump of excess KED and $\Sigma_{\rm HI}$ in the radial range between 170″ and 360″, and again there is no elevated excess $V_{\rm disp}$ there. This region corresponds to the end of the optical spiral arms where there are giant H I complexes (Figure 65 in Walter et al. 2008). Neither of these features in NGC 2976 nor NGC 6946 show up prominently in

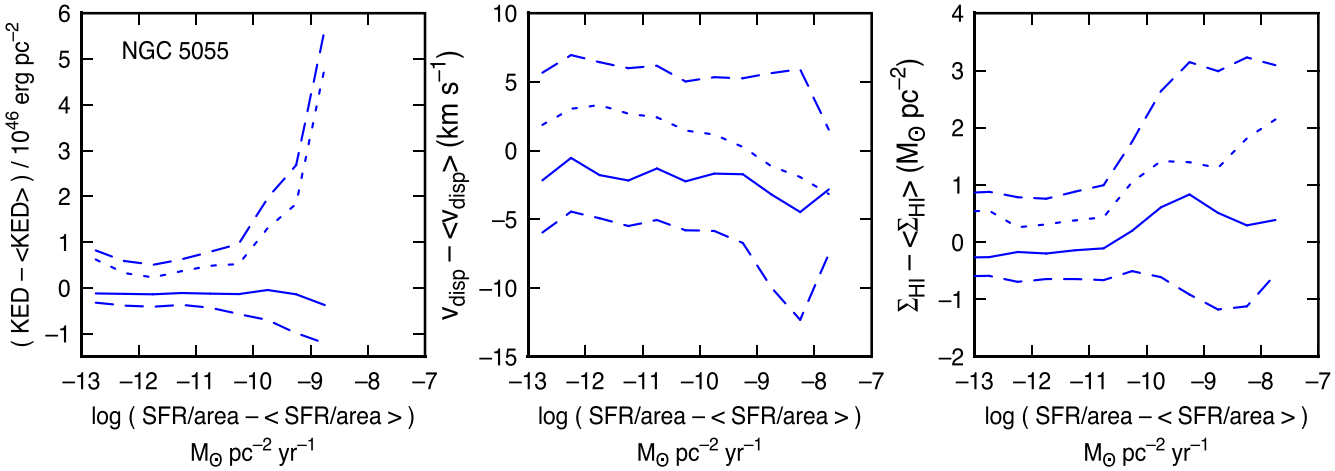

Figure 9. Sample limits for the pixel distributions in Figure 4. The solid lines represent the values of the plotted quantities at the peak densities in the pixel plots, the dashed lines represent the rms deviations of the plotted quantities from their values at the peak densities, and the dotted line is the difference between the positive and negative rms values added to the values at the peak. This dotted line is called the upward bias in the main text, and is taken to be the statistical upper limit. The units for the quantities are the same as in Figure 4.

the average radial profiles in Figure 1; they are excesses relative to this average profile. In about half of the galaxies, the excess SFRD flattens beyond R_{25}, but in these cases, excess $V_{\rm disp}$ shows no indication of a different trend there.

Overall, the radial profiles of the excesses indicate that the correlations or lack of correlations between turbulence generation and local star formation discussed in this paper are for regions beyond the optical disk, which are still relatively bright in FUV and H I. Possible correlations for the main optical disk will show up at the highest excess SFRD, exceeding around −10 in the log with units of $M_\odot$ pc^{-2} yr^{-1}, as indicated by the SFRD excesses to the left of the vertical dotted lines in Figure 8.

3. Analysis

We are interested in how much gas kinetic energy and turbulence each region of star formation generates in its neighborhood on the scale of resolution of the THINGS survey. As mentioned in the previous section, we removed large-scale variations by subtracting the average radial profile of a quantity from the individual pixel values of that quantity, referring to the result as the excess. Figure 4 shows sample plots of excess H I KED, H I $V_{\rm disp}$, and $\Sigma_{\rm HI}$ versus excess SFRD for one galaxy.

There is a lot of scatter in each plot, increasing with higher excess SFRD, but the most common KED excesses and velocity dispersions are small for a wide range of excess SFRD. To quantify these results, we determined four trend lines for each plot. One, representing the most probable correlation, is the excess gas value for each SFRD excess measured at the peak density of pixel points. Another is the rms average of the excess gas value for each excess SFRD measured for all pixel points above the most probable trend line, and a third is the rms average for all pixel points below the most probable trend line. The fourth trend line is the difference between rms above and below the most probable, added to the most probable. This fourth trend is the upward bias from the most probable correlation, and is taken to be indicative of a statistical upper limit of the quantity for each SFRD.

For example, in the case of a KED pixel plot, we made a histogram of the number of points as a function of KED inside each narrow range, ±0.5, of log excess SFRD, where excess SFRD is measured in units of $M_\odot$ pc^{-2} yr^{-1} as in the figures. The excess KED at the peak of the histogram was then determined. Figure 9 shows these most probable trend lines as solid curves. The rms averages above and below the most probable trend lines were determined in the usual way, from the square root of the difference between the average square of the values and the square of the average of the values. These rms averages are the long-dashed curves. The bias trend is shown by a short-dashed curve.

Figure 10 shows the most probable curves in the top panels and the biased or statistical upper limit curves in the bottom panels for each galaxy. The excess KED bias values are mostly positive, so we plot them in log scale in the bottom left panel with each galaxy labeled. The excess KED values themselves hover around zero and are plotted on a linear scale in the upper left. The other panels are linear scale for the most probable and bias values.

The most probable excess KED and $V_{\rm disp}$ values have essentially no dependence on excess SFRD, and are even a little negative for all SFRD, which means that the KED and H I $V_{\rm disp}$ decrease a little in each region of star formation compared to the azimuthal average values. Upper limits to these values, as shown by the bias curves in the bottom row of Figure 10, have a clear upward trend for KED and $\Sigma_{\rm HI}$ and a downward trend for $V_{\rm disp}$. Because KED is half the product of $\Sigma_{\rm HI}$ and the square of $V_{\rm disp}$, the upward trend in KED is entirely from the upward trend in $\Sigma_{\rm HI}$, not from increased turbulent speeds. That is, localized star formation pushes around extra gas in its vicinity, but at lower than average speed. This result applies for all galaxies and SFRDs in the THINGS survey; it is independent of distance, and therefore not likely to result from resolution limits, and it is also independent of size.

From the bottom row of Figure 10, the average slope of the log of the excess KED upper limits versus the log of the excess SFRD is 0.17 ± 0.11. The average slope of the excess $V_{\rm disp}$ upper limits versus the log of the excess SFRD is -0.46 ± 0.87. The average slope of the log of the excess $\Sigma_{\rm HI}$ upper limits (for positive values) versus the log of the excess SFRD is 0.27 ± 0.18. The inverse of this latter quantity is analogous to the Kennicutt–Schmidt relation for H I gas, but here it is for the excess quantities only. We derive

$$d\log(\Sigma_{\rm SFR} - \langle\Sigma_{\rm SFR}\rangle)/ \times d\log(\Sigma_{\rm HI} - \langle\Sigma_{\rm HI}\rangle) = 2.0 \pm 2.0, \quad (1)$$

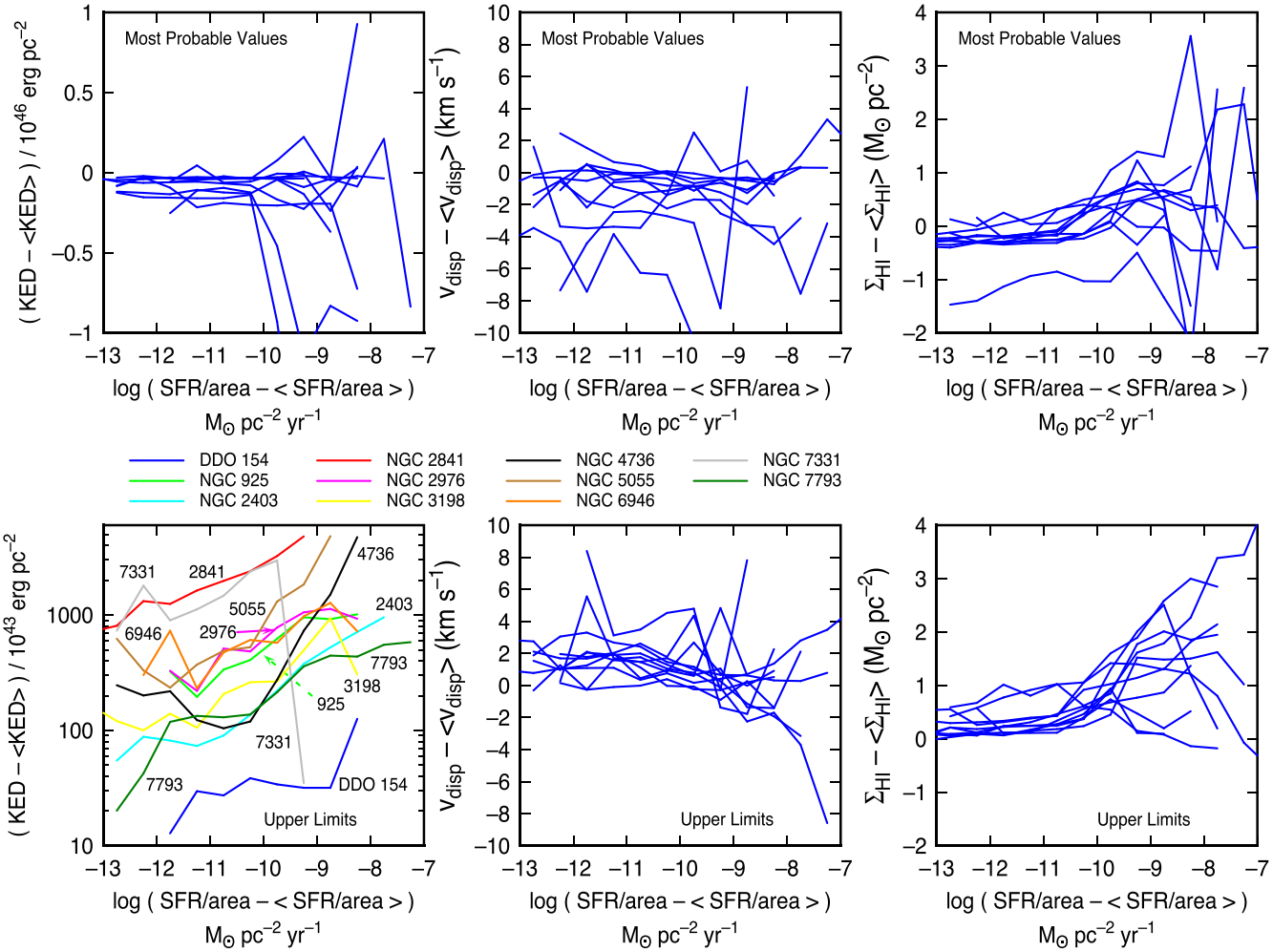

Figure 10. Upper panels show the trend lines for the values of the three quantities at the peaks of the pixel distributions in Figure 4 (solid lines in Figure 9), plotted for all galaxies. Lower panels show the statistical upper limits from the dotted curves in Figure 9 for all galaxies. The upper limits for the excess KEDs are plotted on a log scale with galaxy names indicated and also distinguished by color (only the positive values of excess KED are included because of the log). The units for excess KED are 10^{46} erg pc^{-2} in the top panel and 10^{43} erg pc^{-2} in the bottom panel, $V_{\rm disp}$ is in km s^{-1}, $\Sigma_{\rm HI}$ is in $M_\odot$ pc^{-2}, and excess SFRD is in $M_\odot$ pc^{-2} yr^{-1}. The distributions indicate that the excess KED (top left) is slightly negative for most SFRDs, while the statistical upper limit increases slightly with SFRD (lower left). The excess velocity dispersion is also slightly negative (upper middle), and the upper limit decreases with increasing SFRD (lower middle). The excess H I is slightly negative for small excess SFRD with a slightly increasing trend, and the statistical upper limit to the excess H I is positive and increases with SFRD. One implication of these trends is that the local H I surface density decreases slightly or stays approximately the same in a region of star formation compared to the average value at that radius. Also, the velocity dispersion decreases in regions of star formation, suggesting a slight cooling trend during a conversion to molecules. There is no evidence that feedback from star formation generates turbulence in the local HI gas.

including only positive values of $\Sigma_{\rm HI}$ excess from the upper limit curves. This means omitting all of NGC 6946, which has only negative values. This slope is approximately the same, although with a large uncertainty, as the slope of the KS relation for total H I found for THINGS galaxies by Roychowdhury et al. (2015), also using FUV for the SFR; their slope was 1.65 ± 0.04 on a scale of 1 kpc.

The slope of the excess SFRD versus the excess $\Sigma_{\rm HI}$ could have some bearing on the process of star formation. If we think of the Kennicutt–Schmidt relation as the zero-order correlation in a disk galaxy, involving the bulk gas and the SFRD averaged over many local regions, then an excess correlation as in Figure 10 could be different, showing instead a first-order trend, which might be something relevant to the local rate inside the local regions. Presumably, the zero-order correlation involves the average rate at which bulk gas collects together to make star-forming clouds, in which case a first-order correlation might involve the average rate at which stars form inside the clouds once the clouds have formed. We discussed elsewhere how the zero-order correlation should have a slope of around 1.5 if the gas thickness varies with radius in a galaxy more slowly than the disk surface density, which is usually the case, making the gas thickness approximately constant in the main disk (Gutermuth et al. 2011; Elmegreen 2018; Wilson et al. 2019). The correlation inside self-gravitating clouds could have a different slope, such as ~2, if the cloud thickness depends on its surface density (Elmegreen 2018). Perhaps the correlation between excess $\Sigma_{\rm HI}$ and excess SFRD is hinting at this distinction from the zero-order Kennicutt–Schmidt relation.

4. Fraction of Star Formation Supernova Energy Going into Turbulence

Figure 11 shows the ratio of the excess KED upper limits to the KED expected from 100% of the supernova energy put out by the excess SFRD. This maximum supernova energy is from

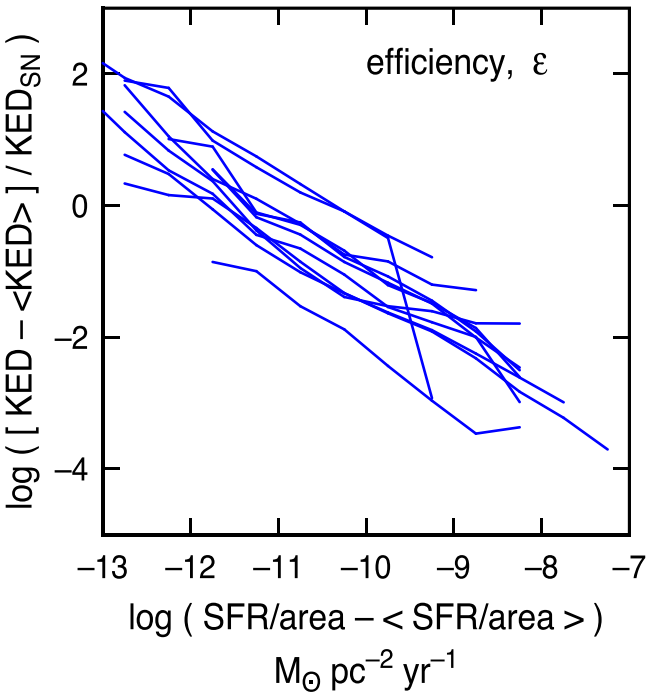

Figure 11. The dimensionless ratio of the upper limit to the excess KED (from the lower left panel of Figure 10) to the hypothetical KED that would come from the excess SFRD at 100% efficiency for supernovae, plotted vs. the excess SFRD. The inverse trend arises because the upper limit to the excess KED varies more slowly than the excess SFRD.

Bacchini et al. (2020),

$$\mathrm{KED_{SN}} = \Sigma_{\mathrm{SFR}} f_{\mathrm{cc}} E_{\mathrm{SN}} (2H/v_{\mathrm{turb}}), \quad (2)$$

where $f_{\mathrm{cc}} = 1.3 \times 10^{-2}\, M_{\odot}^{-1}$ is the number of core-collapse supernovae per solar mass of stars, $E_{\mathrm{SN}} = 10^{51}$ erg is the supernova energy, H is the disk thickness, and v_{turb} is the turbulent velocity dispersion (not the excess turbulent dispersion). The ratio of the observed KED excess to the maximum KED from the excess SFRD is the local-excess analog of the efficiency η in Bacchini et al. (2020). The ratios are plotted versus excess SFRD assuming fiducial values of $H = 100$ pc and $v_{\mathrm{turb}} = 10$ km s^{-1}.

Figure 11 shows a clear trend of η decreasing with increasing excess SFRD. The value of -2 on the ordinate ($\eta = 1\%$) is approximately what Bacchini et al. (2020) got for the average required feedback efficiency, leading them to conclude that there is enough supernova energy to power interstellar turbulence. Here, that value appears again where the *excess* SFRD is about the same as the *average* SFRD in main galaxy disks, i.e., $10^{-9} M_{\odot}$ pc^{-2} yr^{-1}, which is in agreement with Bacchini et al. (2020), but we see systematically higher values for lower excess SFRD. The highest values of η, greater than unity ($\log \eta > 0$) at the lowest excess SFRD, indicate that the excess KED upper limit is more than the excess star formation can generate even at 100% efficiency. This high value is similar to what others get in the outer parts of disks where the SFRD is low (e.g., Tamburro et al. 2009), and it suggests there is an additional source of turbulence. The essential origin of the trend in Figure 11 is that excess KED is more constant than excess SFRD, so the ratio that appears in η varies as the inverse of the excess SFRD. As in Figure 10, the results in Figure 11 suggest that star formation does not significantly influence the KED of local H I.

The lack of a direct correlation between local SFRD and local KED or V_{disp} does not mean there is no feedback, but only that most of the feedback energy does not significantly move local atomic gas. Most of it likely goes into the dense molecular gas, where it radiates efficiently and pumps in gravitational potential energy by pushing apart cloud pieces. The corresponding expansion of the associated H I would then have a relatively low velocity because it is a minor component of the mass. Some of the feedback could also get channeled to remote regions via low-density cavities. For feedback to regulate the SFRD by adjusting the gas scale height, a fraction such as ~1.5% (Bacchini et al. 2020) of all the feedback, not just the local excess, would have to be distributed widely without any significant trace of local or direct agitation by young stars. Regulation of the star formation rate by the break-up of star-forming clouds seems more plausible than adjusting the galactic scale height, given the current results.

5. Conclusions

There is no correlation between excess H I velocity dispersion or excess kinetic energy density and the excess star formation rate per unit area in 11 THINGS galaxies, where excess is defined to be the measured local value minus the azimuthal average value at that position. This result implies that star formation observed in the FUV does not generate significant turbulence in the nearby atomic gas. Either the kinetic energy and momentum generated in the environments of young stars spreads so rapidly over very large regions that it does not show up locally, or this energy and momentum is deposited in a phase of gas that does not show up in the H I survey. Most likely, a significant fraction of the feedback energy from young stars goes into adjacent molecular clouds. Some could also go into cool atomic clouds, such as the debris from shredded molecular clouds, which also would not show up well in the second moment map used here for V_{disp}, because of the narrower linewidths and slower motions of the cool clouds.

There is a slight cooling trend with increasing excess SFRD, in the sense that the statistical upper limits to the excess velocity dispersions decrease systematically with increasing excess SFRD for all galaxies. This trend could correspond to a decay of local H I turbulence before star formation begins in a region, when the gas is condensing into molecular clouds because of self-gravity.

Z.M. appreciates funding from the National Science Foundation (grant Nos. 1852478 and 1950901) to Northern Arizona University for the 2021 Research Experiences for Undergraduates program. We are grateful to the referee for useful comments.

Facility: VLA GALEX.

Appendix
Extended Figures

Pixel-pixel plots of the relative KED (Figure 12), V_{disp} (Figure 13), and Σ_{HI} (Figure 14) values are shown versus the relative excess SFRD for all galaxies in the figures here. The plots for NGC 5055 are also shown in Figure 4. The galaxies are plotted with the same axes scales using colors to indicate the density of pixels on the plot.

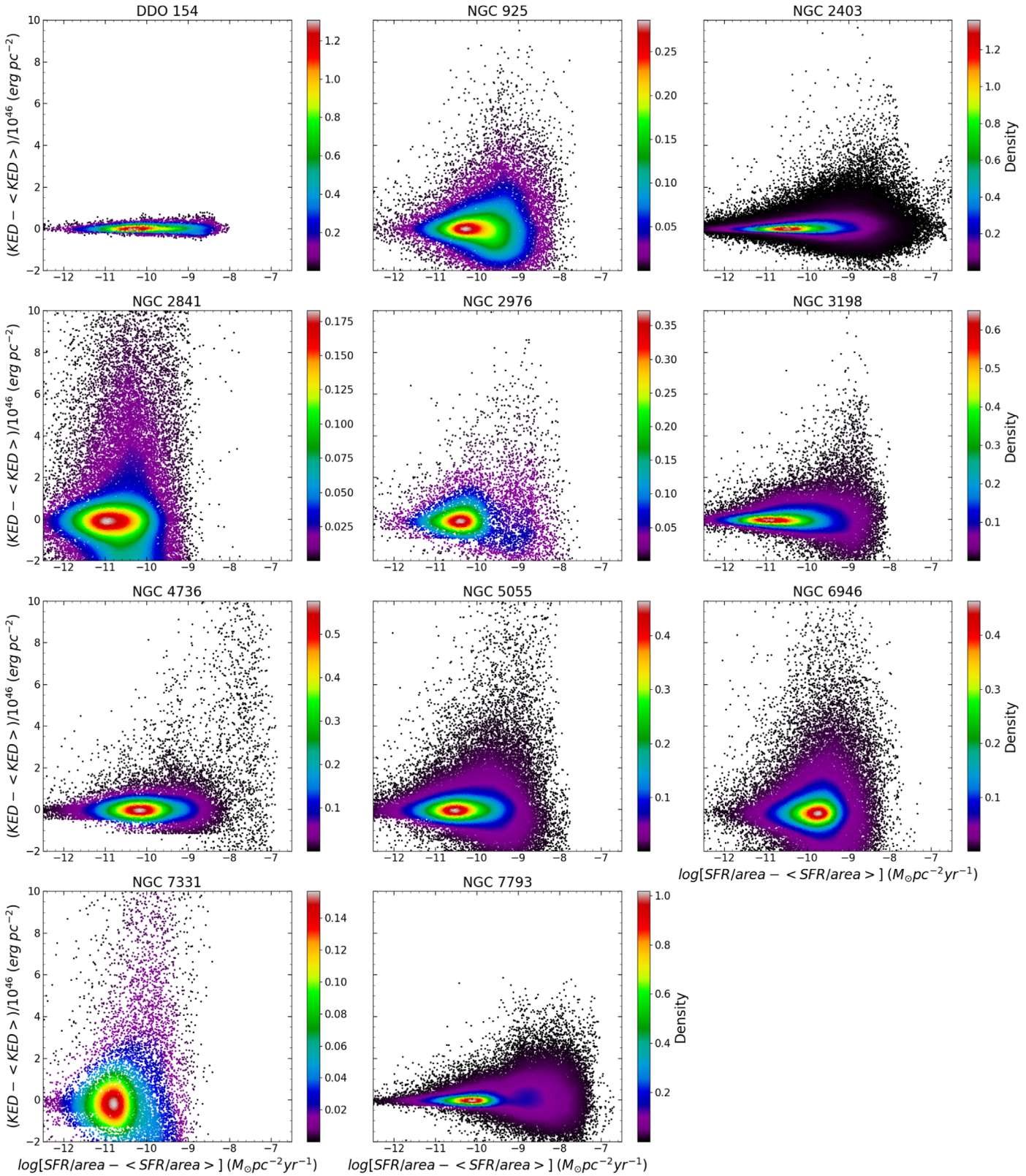

Figure 12. Pixel–pixel plots showing the relationship between the excess KED in units of 10^{46} erg pc^{-2} and the log of the excess SFRD in units of $M_\odot$ pc^{-2} yr^{-1}. The color scale represents the density of points.

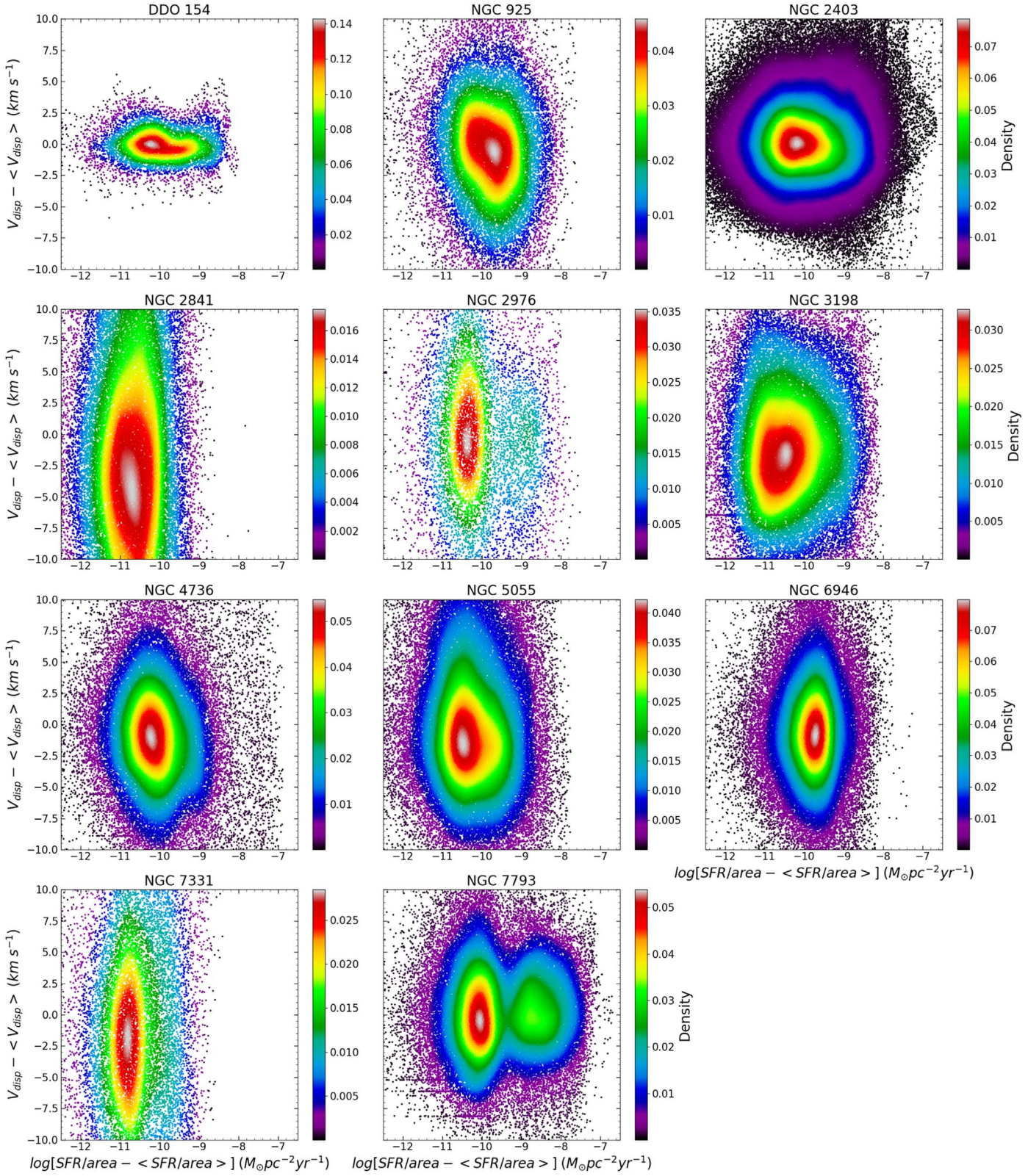

Figure 13. Pixel–pixel plots showing the relationship between the excess $V_{\rm disp}$ in units of km s^{-1} and the log of the excess SFRD in units of $M_\odot$ pc^{-2} yr^{-1}. The color scale represents the density of points.

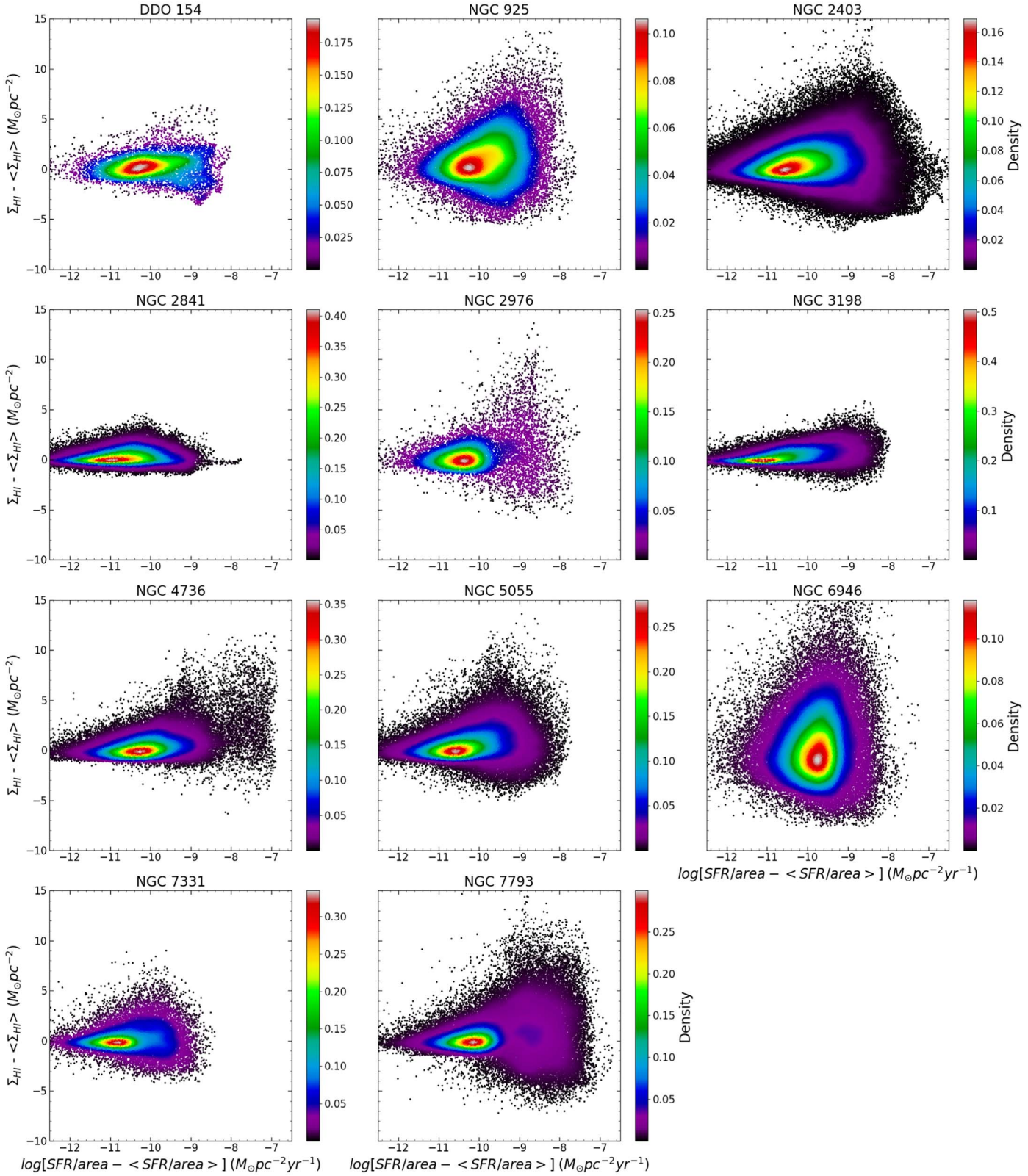

Figure 14. Pixel–pixel plots showing the relationship between the excess $\Sigma_{\rm HI}$ in units of $M_\odot$ pc^{-2} and the log of the excess SFRD in units of $M_\odot$ pc^{-2} yr^{-1}. The color scale represents the density of points.

ORCID iDs

Bruce G. Elmegreen https://orcid.org/0000-0002-1723-6330
Deidre A. Hunter https://orcid.org/0000-0002-3322-9798

References

Agertz, O., Lake, G., Teyssier, R., et al. 2009, MNRAS, 392, 294
Ashley, T., Simpson, C. E., & Elmegreen, B. G. 2013, ApJ, 146, 42
Asseo, E., Cesarsky, C. J., Lachieze-Ray, M., & Pellat, R. 1978, ApJL, 225, L21
Avila-Reese, V., & Vázquez-Semadeni, E. 2001, ApJ, 553, 645
Bacchini, C., Fraternali, F., Iorio, G., et al. 2020, A&A, 641, A70
Balbus, S. A., & Hawley, J. F. 1991, ApJ, 376, 214
Balbus, S. A., & Papaloizou, J. C. B. 1999, ApJ, 521, 650
Bertin, G., & Lodato, G. 2001, A&A, 370, 342
Bournaud, F., Elmegreen, B. G., Teyssier, R., Block, D. L., & Puerari, I. 2010, MNRAS, 409, 1088
Burkhart, B., Stanimirović, S., Lazarian, A., & Kowal, G. 2010, ApJ, 708, 1204
Chevance, M., Kruijssen, J. M., Diederik, H., et al. 2020, MNRAS, 493, 2872
Combes, F., Boquien, M., Kramer, C., et al. 2012, A&A, 539, A67
de Avillez, M. A., & Breitschwerdt, D. 2005, A&A, 436, 585
de Blok, W. J. G., Walter, F., Brinks, E., et al. 2008, AJ, 136, 2648
de Vega, H. J., Sanchez, N., & Combes, F. 1996, Natur, 383, 56
Dib, S., Bell, E., & Burkert, A. 2006, ApJ, 638, 797
Elmegreen, B. G. 2018, ApJ, 854, 16
Elmegreen, B. G., & Burkert, A. 2010, ApJ, 712, 294
Elmegreen, B. G., Elmegreen, D. M., & Leitner, S. N. 2003, ApJ, 590, 271
Elmegreen, B. G., Kaufman, M., & Thomasson, M. 1993, ApJ, 412, 90
Elmegreen, B. G., & Scalo, J. 2004, ARA&A, 42, 211
Franco, J., & Shore, S. N. 1984, ApJ, 285, 813
Gammie, C. F. 2001, ApJ, 553, 174
Gazol, A., & Kim, J. 2010, ApJ, 723, 482
Goldbaum, N. J., Krumholz, M. R., & Forbes, J. C. 2016, ApJ, 827, 28
Goldman, I. 2000, ApJ, 541, 701
Goldreich, P., & Lynden-Bell, D. 1965, MNRAS, 130, 125
Grisdale, K., Agertz, O., Romeo, A. B., Renaud, F., & Read, J. I. 2017, MNRAS, 466, 1093
Gutermuth, R. A., Pipher, J. L., & Megeath, S. T. 2011, ApJ, 739, 84
Hennebelle, P., & Audit, E. 2007, A&A, 465, 431
Hennebelle, P., & Iffrig, O. 2014, A&A, 570, A81
Hodge, P. W., & Hitchcock, J. L. 1966, PASP, 78, 79
Hopkins, P. F., Quataert, E., & Murray, N. 2011, MNRAS, 417, 950
Huber, D., & Pfenniger, D. 2001, A&A, 374, 465
Hunter, D. A., Elmegreen, B. G., & Ludka, B. C. 2010, AJ, 139, 447
Hunter, D. A., Ficut-Vicas, D., Ashley, T., et al. 2012, AJ, 144, 134
Hunter, L. C., van Zee, L., McQuinn, K. B. W., Garner, R., & Dolphin, A. E. 2022, AJ, 163, 132
Joung, M. K. R., & Mac Low, M.-M. 2006, ApJ, 653, 1266
Joung, M. R., Mac Low, M.-M., & Bryan, G. L. 2009, ApJ, 704, 137
Kaufman, M., Brinks, E., Elmegreen, D. M., et al. 1997, AJ, 114, 2323
Kennicutt, R. C., Jr. 1998, ARA&A, 36, 189
Kim, C. G., Kim, W.-T., & Ostriker, E. C. 2006, ApJL, 649, L13
Kim, C. G., Kim, W.-T., & Ostriker, E. C. 2010, ApJ, 720, 1454
Kim, C.-G., Ostriker, E. C., & Kim, W.-T. 2013, ApJ, 776, 1
Kim, W.-T., & Ostriker, E. C. 2007, ApJ, 660, 1232
Kim, W.-T., Ostriker, E. C., & Stone, J. M. 2002, ApJ, 581, 1080
Kim, W.-T., Ostriker, E. C., & Stone, J. M. 2003, ApJ, 599, 1157
Krumholz, M., & Burkert, A. 2010, ApJ, 724, 895
Li, Y., Mac Low, M.-M., & Klessen, R. S. 2005, ApJL, 620, L19
Mac Low, M.-M., & Klessen, R. S. 2004, RvMP, 76, 125
Martin, D. C., Fanson, J., Schiminovich, D., et al. 2005, ApJL, 619, L1
Nath, B. B., Das, P., & Oey, M. S. 2020, MNRAS, 493, 1034
Norman, C. A., & Ferrara, A. 1996, ApJ, 467, 280
Orr, M. E., Hayward, C. C., Medling, A. M., et al. 2020, MNRAS, 496, 1620
Ostriker, E. C., McKee, C. F., & Leroy, A. K. 2010, ApJ, 721, 975
Parker, E. N. 1966, ApJ, 145, 811
Piontek, R. A., & Ostriker, E. C. 2007, Apj, 663, 183
Renaud, F., Bournaud, F., Kraljic, K., & Duc, P.-A. 2014, MNRAS, 442, L33
Richard, D., & Zahn, J. 1999, A&A, 347, 734
Roychowdhury, S., Huang, M.-L., Kauffmann, G., Wang, J., & Chengalur, J. N. 2015, MNRAS, 449, 3700
Sellwood, J. A., & Balbus, S. A. 1999, ApJ, 511, 660
Semelin, B., & Combes, F. 2000, A&A, 360, 1096
Shetty, R., Vogel, S. N., Ostriker, E. C., & Teuben, P. J. 2007, ApJ, 665, 1138
Stilp, A. M., Dalcanton, J. J., Skillman, E., et al. 2013a, ApJ, 733, 88
Stilp, A. M., Dalcanton, J. J., Warren, S. R., et al. 2013, ApJ, 772, 124
Szotkowski, S., Yoder, D., Stanimirović, S., et al. 2019, ApJ, 887, 111
Tamburro, D., Rix, H.-W., Leroy, A. K., et al. 2009, AJ, 137, 4424
Tenorio-Tagle, G. 1981, A&A, 94, 338
Tody, D. 1986, Proc. SPIE, 627, 733
Trachternach, C., de Blok, W. J. G., Walter, F., Brinks, E., & Kennicutt, R. C., Jr. 2008, AJ, 136, 2720
Vollmer, B., & Beckert, T. 2002, A&A, 382, 872
Wada, K., Meurer, G., & Norman, C. A. 2002, ApJ, 577, 197
Walker, A., Gibson, B., Pilkington, K., et al. 2014, MNRAS, 441, 525
Walter, F., Brinks, E., de Blok, W. J. G., et al. 2008, AJ, 136, 2563
Wilson, C. D., Elmegreen, B. G., Bemis, A., & Brunetti, N. 2019, ApJ, 882, 5
Zhang, H.-X., Hunter, D. A., & Elmegreen, B. G. 2012, ApJ, 754, 29